PHYSICAL SCIENCES

Compressing slippery surface-assembled amphiphiles for tunable haptic energy harvesters

Pallav K. Jani[1], Kushal Yadav[1], Maryanne Derkaloustian[2], Hilmar Koerner[3], Charles Dhong[2,4], Saad A. Khan[1]*, Lilian C. Hsiao[1]*

A recurring challenge in extracting energy from ambient motion is that devices must maintain high harvesting efficiency and a positive user experience when the interface is undergoing dynamic compression. We show that small amphiphiles can be used to tune friction, haptics, and triboelectric properties by assembling into specific conformations on the surfaces of materials. Molecules that form multiple slip planes under pressure, especially through π-π stacking, produce 80 to 90% lower friction than those that form disordered mesostructures. We propose a scaling framework for their friction reduction properties that accounts for adhesion and contact mechanics. Amphiphile-coated surfaces tend to resist wear and generate distinct tactile perception, with humans preferring more slippery materials. Separately, triboelectric output is enhanced through the use of amphiphiles with high electron affinity. Because device adoption is tied to both friction reduction and electron-withdrawing potential, molecules that self-organize into slippery planes under pressure represent a facile way to advance the development of haptic power harvesters at scale.

INTRODUCTION

Energy-harvesting technologies that collect ambient energy from human motion are revolutionizing self-sustaining wearable electronics for applications in healthcare, communications, and haptic manipulation in augmented and virtual reality (*1*–*6*). Triboelectrification is one such energy-harvesting method and operates by charge transfer between the electronic device and human skin, a process that relies on adhesion and friction. However, most materials and dopants cannot simultaneously produce high charge densities, maintain haptic comfort, and be produced economically at scale. Developing a library of materials with tunable solid-solid friction would enable widespread adoption and extended wear of tactile energy harvesters by increasing performance (*7*, *8*) and comfort, a key design consideration for wearables akin to clothing selection (*9*). Most humans perceive materials with low kinetic friction coefficients μ_K as having a pleasant sensation (*10*, *11*).

Physicochemical modification of the material interface, for example, through organic and inorganic molecules, patterned textures, and surface interactions, is a common strategy to improve tactile perception (Fig. 1A) (*12*–*14*). Nevertheless, the multifaceted nature of friction makes it challenging to develop friction reduction and triboelectric strategies for soft materials (*15*), and, therefore, how the interface might be engineered for wearable energy harvesters remains poorly understood. This study shows how tactile perception and energy harvesting can be tuned by a single C═C bond on a small amphiphilic molecule that self-assembles into ordered layers at the interface and, furthermore, provides an original and universal physical model for how friction is reduced by pressure-induced changes in these self-assembled slip layers.

Small amphiphiles meet the unique requirements of ambient energy harvesters, serving as facile and benign dopants in many polymer systems, and are of substantial interest to a broad audience including materials scientists, engineers, and technologists. These organic molecules migrate to the surface and self-assemble into robust, slippery interfacial multilayers that minimize solid contact and reduce μ_K (*16*). Their electron affinity can also be tuned with respect to the underlying substrate to maximize the surface charge density (*17*). Recent advancements in molecular-scale surface modifications to alter friction have resulted in distinct surface tactile perceptions (*13*, *18*). In particular, self-assembled layers of aliphatic amphiphiles have been used to make wearable devices more comfortable (*19*). Besides improving energy-harvesting performance, slip additives should also provide a pleasant sensation, which is highly dependent on surface chemistry differences on the order of a single monolayer (*13*). Most studies focus on doping materials with Young's modulus $E > 10^3$ MPa (*20*–*22*) in order to prevent wear and material transfer of the hard polymer tribolayer in triboelectric devices (*23*).

Here, we focus on the friction, triboelectric, and haptic properties for materials of different moduli ($10^0 < E < 10^5$ MPa) treated with multilayers of model amide-based amphiphiles. The first molecule, erucamide (ER; Fig. 1B), is a C_{22} aliphatic amide that substantially reduces friction for polymer-metal tribopairs. Its backbone contains an unsaturation site capable of π-π stacking to form ordered mesoscale stacks. The second amphiphile is behenamide (BE; Fig. 1B), the saturated counterpart of ER, which traditionally shows a much lower effectiveness in friction reduction (*20*). Our goal is to quantify and explain the observed differences between ER and BE on various surfaces. Multiple hypotheses have been proposed for the effectiveness of amphiphilic slip additives, including interfacial shear strength (*24*), adhesion (*25*), slip planes (*26*, *27*), structural order, and surface coverage (*28*). Simulations suggest that the high μ_K for BE stems from the lack of a π-bond, causing molecular chains to be distributed in spread-out configurations that fail to prevent intimate tribopair contact (*28*). Experimental observations support the idea that the work required to shear "bumpy" hard BE crystals is much greater than that for plate-like soft ER crystal (*20*).

[1]Department of Chemical and Biomolecular Engineering, North Carolina State University, Raleigh, NC, USA. [2]Department of Materials Science and Engineering, University of Delaware, Newark, DE, USA. [3]Air Force Research Laboratory, RXNP, Wright-Patterson Air Force Base, Fairborn, OH, USA. [4]Department of Biomedical Engineering, University of Delaware, Newark, DE, USA.
*Corresponding author. Email: lilian_hsiao@ncsu.edu (L.C.H.); khan@eos.ncsu.edu (S.A.K.)

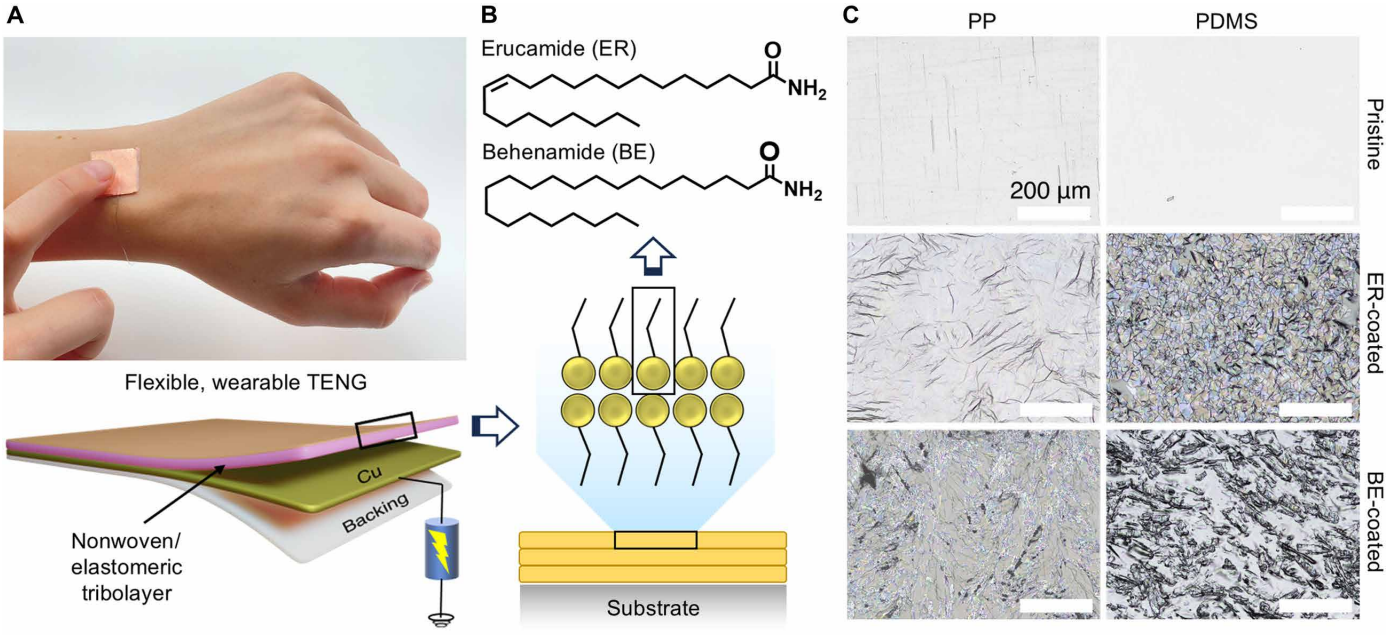

Fig. 1. Interfacial modification by small amphiphiles. (**A**) Photograph depicts a user tapping a flexible, wearable triboelectric device composed of a conformal backing, a thin Cu film as a collecting electrode, and a flexible nonwoven or elastomer as the tribolayer. Modification of the tribolayer by interfacial additives creates distinct haptic sensations and triboelectric signals. (**B**) Molecular structures of the two amphiphilic additives, erucamide (ER) and behenamide (BE). Schematic illustrating the fabrication of multilayered fatty amide-based coatings with stacks of bilayers due to the tendency of fatty amides to form dimers. (**C**) Optical images of the pristine, ER-coated, and BE-coated PP and PDMS substrates showing near-complete coverage of the slip additive on the surface.

Adhesive friction is a critical aspect in the coupled challenge of friction, haptics, and triboelectric generation. Derjaguin described its effect on slipperiness, or the interfacial friction force F_F, as

$$F_F = \tau_0 A_c + \alpha F_N \quad (1)$$

The first term is the adhesion force that depends on the interfacial critical stress τ_0 and the contact area A_c, while the second term is a kinetic friction force that scales with normal load F_N (*29*, *30*). Dividing Eq. 1 by F_N yields a more useful form for material design

$$\mu_K = \tau_0/P + \alpha \quad (2)$$

where P is the applied pressure and α represents the lowest possible friction for a given additive (*24*). Equation 2 is a powerful design relation stating that low adhesive friction is achievable by decreasing τ_0 of the slip layers or by increasing P (*24*), directly implying the importance of tribopair elasticity (*31*) alongside slip additive shear strength. While similar frictional laws exist for many amphiphiles (*22*, *31*, *32*), how amide-based slip additives influence Eq. 2 at a molecular level is unclear. Consequently, selecting a proper molecule for lubrication remains arbitrary without a complete knowledge of how it reduces friction under various tribological stresses (*33*). ER and BE were specifically chosen here for their propensity to assemble into stacks of different configurations, allowing us to understand how mesoscale structures formed under high pressure reduce μ_K for a broad range of materials with different chemistry and elasticity.

RESULTS

Reducing friction with slip additives

ER slip layers generated substantially greater friction reduction in a range of tribopairs. The slip layers were created by solvent-assisted casting (see Materials and Methods) to form diverse tribopair combinations, including polypropylene-polypropylene (PP-PP), PP-silicon wafers, PP–low-density polyethylene (LDPE), PP-polydimethylsiloxane (PDMS), PDMS-PDMS, and polyurethane-PP nonwovens that emulate skin-textile contact (*34*). These tribopairs spanned three orders of magnitude in the reduced elastic moduli ($E^* = 10^0$ to 10^3 MPa; table S1). The coated substrates were analyzed using Fourier transform infrared (FTIR) spectroscopy in attenuated total reflectance mode to detect amide groups, visible as absorbance peaks at 3360 and 3184 cm^{-1} (—NH_2 stretching) and at 1646 cm^{-1} (—C═O stretching) (fig. S1) (*35*). Optical images of the coated substrates in Fig. 1C and fig. S1 show near-complete additive surface coverage, where the additive layer is ~3.8 ± 1.01 μm thick with a root mean square roughness of $S_q = 0.71 \pm 0.22$ μm [figs. S2 and S3 and Supplementary Text (ST) section 2]. The micrometer-thick layers indicate that ER and BE self-assembled into multiple stacks of bilayers through hydrogen bonding (*25*).

Boundary friction of pristine and coated tribopairs was tracked using a stress-controlled triborheometer with a ball-on-plate contact (fig. S4), sheared at a constant speed of 5 mm/s over 3600 s under $F_N = 0.7$ to 35.3 N (table S2). Figure 2A shows that ER reduced the steady-state friction coefficient $\bar{\mu}_K$ by 81% in PP-PP tribopairs, reducing the value from $\bar{\mu}_K = 0.39 \pm 0.01$ (pristine) to $\bar{\mu}_K = 0.07 \pm 0.01$ (ER coated), similar to coated polyethylene-metal systems in the literature (*20*). This reduction was found across all tribopairs and F_N values (fig. S5), including nonwovens paired with a polyurethane skin simulant with skin-like roughness ($S_q = 6.7 \pm 0.1$ μm) (*34*). In the specific case of nonwovens, an annular ring-on-plate contact simulated the large-area textile-skin rubbing process (fig. S6). ER was highly effective at friction reduction with stiff PP substrates but showed only a modest 52% reduction with nonwovens

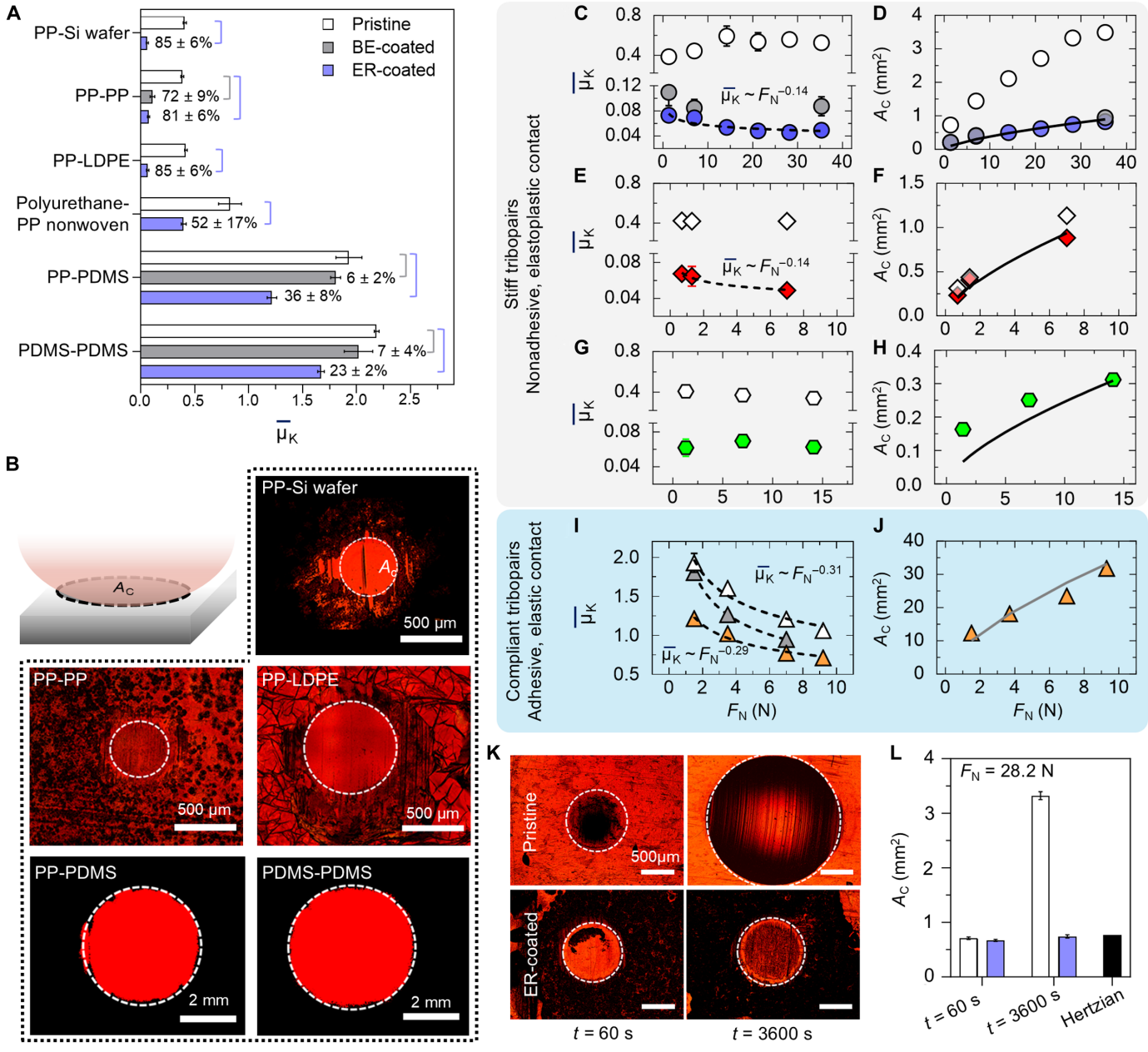

Fig. 2. Friction, contact, and wear of tribopairs. (**A**) ER and BE interfacial layers produced different degrees of friction reduction for different tribopairs. Percentages represent the relative friction reduction for coated tribopairs. (**B**) Representative optical images (PP-PP, PP-LDPE, and PP-Si wafer) and thresholded confocal microscopy images (PP-PDMS and PDMS-PDMS) of the apparent contact area (A_c) on ER-coated substrates at F_N = 1.4 N after t = 3600 s of sliding. Dashed lines are to guide the eye. Dependence of $\bar{\mu}_K$ and A_c on F_N for pristine (open), ER-coated (closed, colored), and BE-coated (closed, gray) tribopairs of (**C** and **D**) PP-PP, (**E** and **F**) PP-LDPE, (**G** and **H**) PP-Si wafer, and (**I** and **J**) PP-PDMS. Dashed lines represent power law fits. Solid lines represent the theoretical Hertzian contact area for stiff, nonadhesive tribopairs and the Johnson-Kendall-Roberts (JKR) contact area for the compliant, adhesive tribopair. (**K**) Representative optical images and (**L**) A_c measurements of the PP-PP tribopairs at F_N = 28.2 N, illustrating the wear protection by slip additives.

($\bar{\mu}_K = 0.82 \pm 0.11$ for pristine nonwoven and $\bar{\mu}_K = 0.39 \pm 0.02$ for coated nonwoven) that further decreased to 23% for the soft PDMS-PDMS tribopairs. Similar variations were found in BE-coated systems, with comparable friction reduction as ER for PP but notably worse effectiveness with PDMS (7%). In general, the same slip additive produced different extents of friction reduction with different tribopairs (Fig. 2A), suggesting that the frictional dissipation mechanism may also be related to the substrate modulus.

Balancing adhesion and normal load

The friction reduction mechanism depends on the nature of the contact area between the substrates because pressure exerted on slip planes at a molecular level influences their structure and conformation. Amontons' first law, which states that F_F should scale linearly with F_N (*36*), is seen in stiff, pristine tribopairs with $E^* > 10^2$ MPa (fig. S7A). ER-coated stiff tribopairs demonstrated a slight deviation from Amontons' first law, with the exception of PP-Si wafers, as the

softer slip layers may introduce elastic character to the stiff interface (Fig. 2, C, E, and G, and ST section 3) (*32*, *36*, *37*). All pristine and coated tribopairs are nonadhesive in nature (figs. S7, A to C) (*32*).

Soft adhesion ($E^* < 10^1$ MPa) leads to deviation from Amontons' first law where $\bar{\mu}_K$ showed a strong power-law dependence on F_N for both pristine and coated PDMS substrates (exponents = −0.29 to −0.39; Fig. 2I). PDMS is a model elastomer system with adhesive properties, showing a finite F_F when $F_N = 0$ (figs. S7, D to F) (*32*); our reported scaling exponents are also similar to many reported PDMS tribopairs (−0.33 to −0.55) (*38*, *39*). The scalings indicate conformal contacts because the real contact area approaches the apparent contact area A_c, and, as a result, F_F scales linearly with A_c (*15*, *31*). Direct imaging of the apparent contact areas (Fig. 2B, figs. S8 to S10, and ST section 4) showed that A_c values for nonadhesive coated tribopairs agreed with the Hertzian model (Fig. 2, D, F, and H). The adhesive Johnson-Kendall-Roberts (JKR) model extends Hertzian model in describing adhesive contacts with an added surface energy and predicted A_c values for PP-PDMS tribopairs (Fig. 2J and ST section 5). Data of F_F against A_c for coated PDMS and nonwoven systems collapsed on a single linear fit (fig. S11C), providing further evidence of adhesive, contact area-dependent friction in soft contacts (*31*, *32*).

Figure 2 shows that a larger contact area, caused by either softness or adhesion between tribopairs, tends to render the slip additives less effective. Both fatty amides were only moderately successful at shielding the adhesive interactions that govern the sliding friction of soft materials. Nevertheless, they minimized wear by minimizing ploughing during compressive sliding as opposed to pristine substrates that underwent visible wear (Fig. 2, K and L; figs. S9, S12, and S13; and ST section 6). The negligible wear validates the use of Derjaguin's model for the friction dissipation mechanism (*40*).

Slipping under pressure

The different classifications of contact areas in Fig. 2 (C to J) correlate with the distinction between adhesive and load-dominant regimes for slip additives (*31*, *40*, *41*). Figure 3 shows that this transition occurs at a relatively low pressure ($P \sim 1$ MPa) as compared to physisorbed coatings on metals ($P = 50$ MPa) (*40*). One explanation is that pressure induces changes in the slip planes, consisting of aliphatic chains facing one another (*24*), which evolve during dynamic sliding and dissipate shear stresses as shown from the scaling of τ_F with P (fig. S14). At low P, attractive van der Waals forces localize the sliding plane to the topmost interfacial layer (Fig. 3A, top left), giving rise to interfacial critical stress values of $\tau_0 = 0.14$ MPa for ER and $\tau_0 = 0.21$ MPa for BE that are substantially lower than the critical stresses of pristine polymer contacts (*16*, *22*, *36*). BE slip layers are likely more disordered in their molecular configuration than ER due to the lack of a π-bond (*28*), which causes chains to interdigitate, hence increasing the shear stress required to maintain sliding.

We confirmed the differences in the structural ordering of ER and BE by performing grazing-incidence x-ray scattering, a highly surface sensitive technique, over a range of wave vectors (q) on slip additive-coated PDMS substrates (Materials and Methods and fig. S15). Grazing-incidence wide-angle x-ray scattering (GiWAX) and grazing-incidence small-angle x-ray scattering (GiSAX) images and

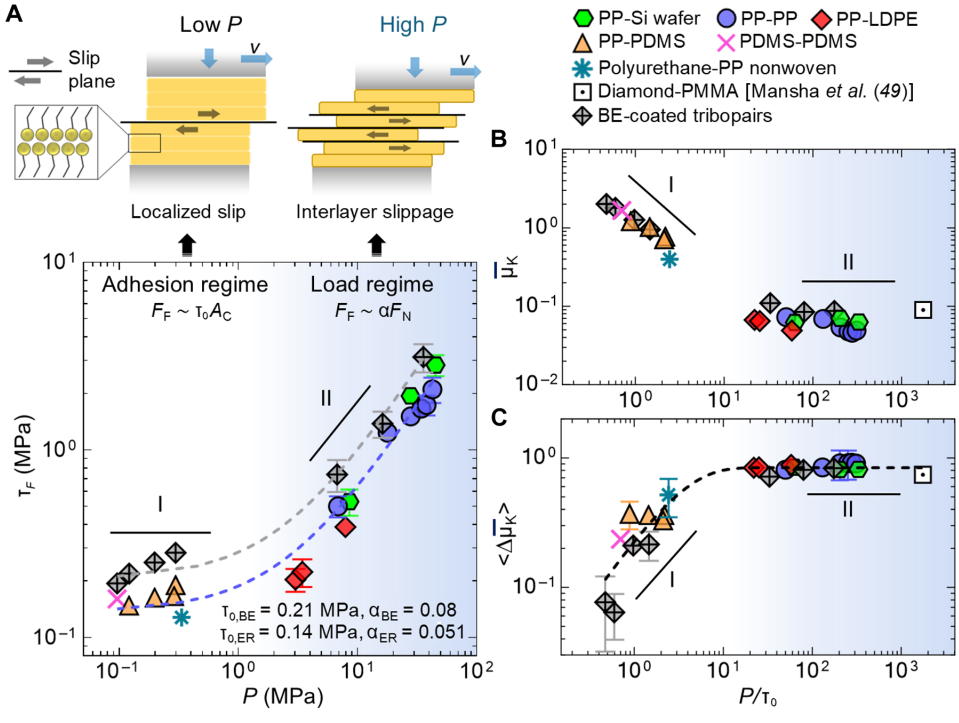

Fig. 3. Distinct scaling regimes due to pressure-induced changes of slip layers. (**A**) τ_F-P relationship for ER-coated and BE-coated tribopairs demonstrates two distinct frictional regimes: an adhesion regime (I) and a load regime (II). At low P, τ_F is independent of P due to adhesive interactions at localized slip planes (top left). At high P, τ_F scales with P and multiple interlayer slip planes form within the slip additive multilayered structure (top right). Dashed lines represent linear fits based on Eq. 1 normalized by A_c to extract specific τ_0 values for each slip additive. (**B**) Plot of $\bar{\mu}_K$ for coated tribopairs as a function of the normalized pressure, P/τ_0. (**C**) Friction reduction $<\Delta\bar{\mu}_K>$ as a function of P/τ_0 for ER and BE collapse onto a single exponential plateau–type fitting (dashed line). Error bars represent SDs from three independent measurements.

intensity spectra show that both ER and BE have an intensity peak at wave vector $q = 0.145$ Å^{-1} (fig. S15C), which corresponds to a length scale of 4.3 nm, characteristic of tilted, amide bilayers (*25*, *42*). ER self-assembles into higher, well-ordered structures spanning several millimeters into the film as evidenced by multiple crystalline peaks (fig. S15D). On the contrary, BE forms only a weak bilayer with the overall structure remaining mostly isotropic and liquid-like over larger length scales, supporting the statement that the C═C bond within the ER backbone is crucial for the formation of ordered slip layers and mesodomains (detailed description of GiWAX and GiSAX analysis is provided in ST section 7). Consequently, ER outperformed BE in the adhesive regime, where P was comparable to τ_0, and the frictional dissipation is mainly from the first term of Eq. 2 (fig. S16, B and C).

Slip additives lost effectiveness when the applied pressure is less than the critical interfacial stress ($P/\tau_0 < 1$), shown from the increase in the average kinetic friction $\overline{\mu}_K$ and lower friction reduction $<\Delta\overline{\mu}_K>$ at very low P (Fig. 3, B and C). This is because larger contact areas, characteristic of soft tribopairs, increase the total number of adhesive interactions at the localized slip planes (*43*), and more energy is needed to maintain sliding. Thus, $\overline{\mu}_K$ and $<\Delta\overline{\mu}_K>$ scale with P/τ_0 in the adhesive regime.

As P increases toward the load regime, the friction-reducing effectiveness $<\Delta\overline{\mu}_K>$ also increases. BE and ER exhibited nearly identical friction behavior (fig. S16A). Elevated pressures ($P/\tau_0 >> 1$) can cause the interfacial layers to compress and densify (*36*, *44*, *45*), disrupting adhesive interactions and creating multiple interlayer slip planes (Fig. 3A, top right) that effectively dissipate frictional stresses. This type of slip is responsible for the ultralow friction of graphene (*46*), molybdenum sulfide nanosheets (*47*), and ice, where an interfacial premelting film formed under compression is thought to provide lubrication (*48*).

A pressure-invariant plateau in $<\Delta\overline{\mu}_K>$ at 84 ± 5% was evident for all coated stiff tribopairs (Fig. 3C), in agreement with literature reports on ER-coated diamond-polymethylmethacrylate tribopairs (*49*). While literature on amphiphilic layers has primarily focused on metal surfaces and the use of nanoscale tribology to identify their frictional dissipation properties (F_F versus F_N and F_F versus A_c) (*22*, *41*), a general framework to correlate the frictional dissipation to the friction reduction capacity of amphiphiles is lacking. In addition, only a few studies have expanded the understanding of self-assembled layers on polymeric surfaces. (*20*, *25*). Here, we show that, for stiff substrates, both $\overline{\mu}_K$ and $<\Delta\overline{\mu}_K>$ varied only marginally, irrespective of the choice of material or slip additive, indicating that (i) the creation of interlayer slip planes under high pressure negates the influence of the underlying substrate and the slip additive structure (*45*), and (ii) there exists an upper limit to friction reduction induced by this mechanism. While computer simulations have been used to understand the organization of amphiphiles under pressure on metal surfaces (*26*, *33*), direct experimental evidence of pressure induced interlayer slippage is challenging due to the need for a specialized equipment to monitor both the friction and structural changes simultaneously. Future work using a custom in operando shear cell mounted onto either x-ray scattering or diffraction instrument could enable real-time monitoring of the slip layers under pressure.

The friction reduction capacity of amide-based slip additives is represented by an empirical expression of the form $\langle \Delta\overline{\mu}_K \rangle = a\left(1 - e^{-bP/\tau_0}\right)$ (Fig. 3C), where $a = 0.84$ signifies the maximum achievable friction reduction and $b = 0.31$ is a fitting parameter indicating the rate of change in friction reduction with the dimensionless pressure. The variable P/τ_0 is reminiscent of the pressure term P/σ_y, where P is normalized by the material yield strength σ_y and $P/\sigma_y >> 1$ indicates irreversible plastic deformation under pressure (*37*). In this study, $P/\tau_0 >> 1$ suggests the onset of interlayer slippage within the slip layers. The scaling expression encompasses friction reduction of ER and BE across various materials, offering a framework for understanding slip additive performance, especially for soft materials. For instance, suppose that an application specifies a friction reduction target using a specific slip additive. This framework can help identify appropriate tribological pressures and materials or, conversely, predict the friction reduction for a given set of operating conditions. The reported friction coefficients, shear stresses, and pressures in Fig. 3 are mean field quantities that are averaged over the contact gap, where the normal pressure is assumed to be symmetric around the center as suggested by Hertzian and JKR mechanics. During sliding motion, a nonuniform pressure distribution may lead to the von Mises stresses to be greatest near the front of the sliding object (*50*). Higher local pressures within the contact may then lead to potentially increased molecular ordering locally; however, the measured bulk values in this study average over any local variations in the gap. Our results also pertain to slip layers with near-complete surface coverage. At partial coverage or exceedingly high pressures (P on the order of GPa), slip additives may be squeezed out of the contact zone during sliding. Friction reduction may then be confounded by time-dependent wear and the junction strength of pristine regions within the contact area (*51*).

Human perception and triboelectric performance

Few humans are willing to tolerate devices and clothing that generate high frictional forces. The widespread adoption of wearable triboelectric devices relies on energy-harvesting performance in conjunction with extended usage by the populace. Given that emerging devices often incorporate adhesive PDMS layers (*52*), the question arises: Do the observed frictional differences between ER and BE on PDMS change tactile perception and the user experience?

We first assessed whether humans could reliably distinguish between different pairs of pristine and coated PDMS substrates using a three-alternative forced choice (3-AFC) or "odd-man-out" method (Fig. 4A and movie S1) (*18*). Participants, blindfolded to prevent visual cues, were presented with three randomly placed samples and asked to correctly identify the unique sample. This task was performed five times per pair on fresh samples and provided objective performance measures in tandem with a more subjective assessment of which surface felt better on the skin.

ER emerged as the clear winner in generating a pleasant tactile sensation. Figure 4B shows that participants could differentiate between the pristine and coated PDMS surfaces above random chance ($P < 0.001$), implying that both slip additives substantially altered the tactile perception. All participants consistently distinguished between pristine and ER-coated PDMS (25 of 25 trials) but had lower success distinguishing between the two slip additives [88%, 70.0 to 95.8% with 95% confidence interval (CI), Wilson score intervals] and between pristine and BE-coated PDMS (80%, 60.8 to 91.1% with 95% CI). This reduced tactile accuracy trend is likely due to a reduced frictional change, as measured among the pristine and coated PDMS tribopairs in the friction tests at low pressures of 0.08 to 0.1 MPa (Fig. 4B), which is slightly higher than the range of fingertip sliding pressures (0.003 to 0.03 MPa) (*18*, *53*, *54*). Nolin *et al.*

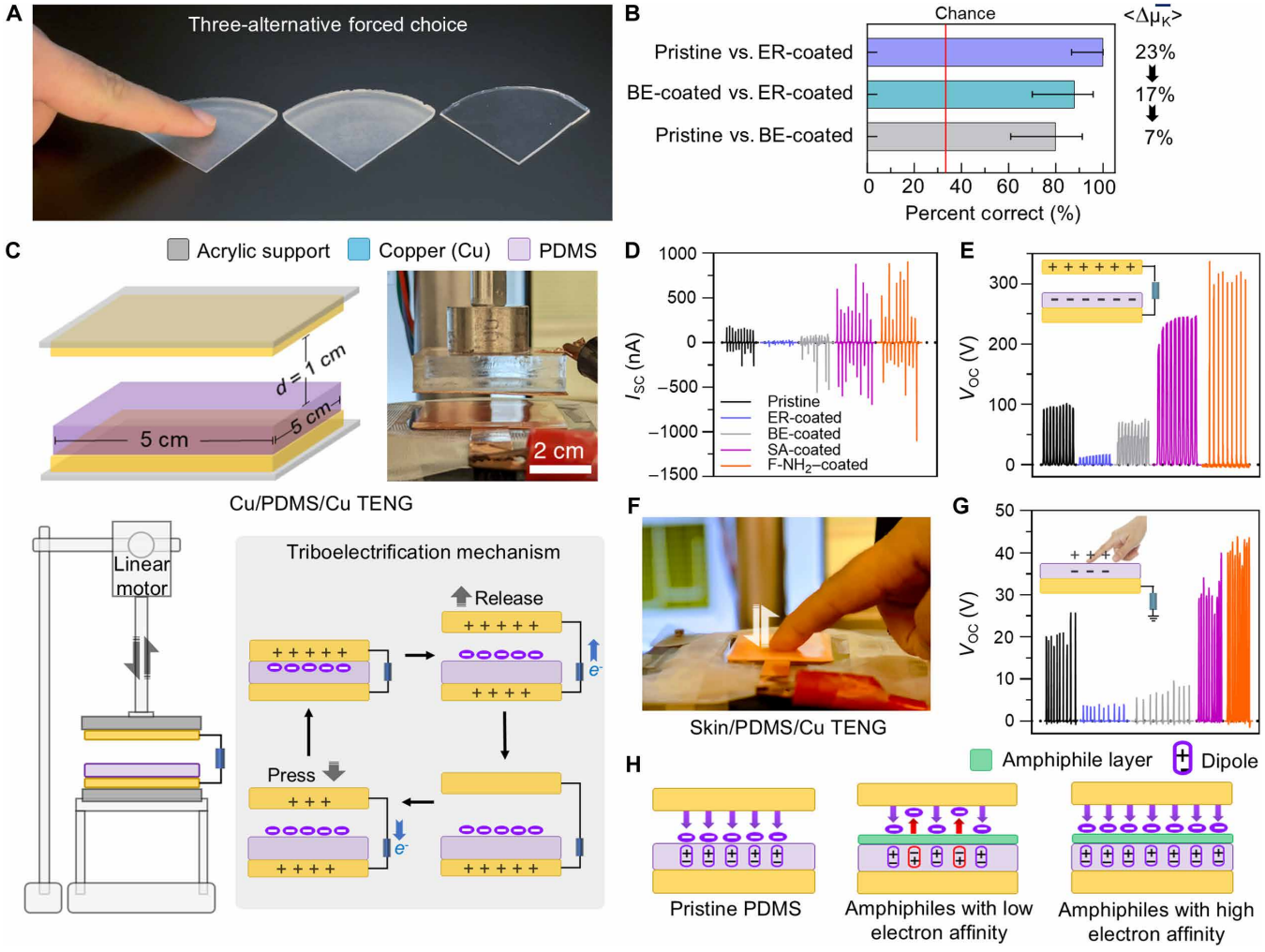

Fig. 4. Human tactile perception and triboelectric tuning by self-assembled layers on PDMS. (**A**) A participant explores the PDMS surface with their index finger in a three-alternative forced choice (3-AFC) trial to identify the "odd-man-out" from two identical and one different substrate that are randomized in identity and placement. (**B**) Participant responses to the 3-AFC task for different pairs of pristine and coated PDMS. Red line corresponds to guessing by chance, and $<\Delta\bar{\mu}_K>$ denotes average friction reduction between pair. The number of data points is $n = 25$, obtained from five participants for each pair. Error bars represent 95% confidence intervals calculated by Wilson score intervals. (**C**) Left: Setup for a 50 mm–by–50 mm Cu/PDMS/Cu triboelectric device operating in the contact-separation mode (10 cycles, 0.3 Hz) with a Cu plate as the positive tribomaterial and PDMS as the negative tribomaterial. Right: Schematic of the triboelectrification. (**D**) I_{SC} and (**E**) V_{OC} measurements show that the amphiphilic molecules induce distinct triboelectric signals compared to the pristine surface. (**F**) Skin/PDMS/Cu triboelectric device in tapping mode with the finger acting as the positive tribomaterial and the resulting (**G**) V_{OC} signals. (**H**) Proposed molecular mechanism of triboelectric tuning by amphiphiles.

(*18*) have previously shown that a transition in the surface layer brought about by chemical substitution translates into sharp frictional change and, hence, haptic contrast. Similarly, in the low P regime, the differences in the interfacial stress (τ_0) (Fig. 4A) and, hence, the friction generated by the localized slip plane of ER and BE in comparison to the pristine PDMS surface likely affected the haptic contrast between the surfaces. When participants were further asked to subjectively rank the three substrates based on tactile preference, 80% identified ER-coated PDMS as their most preferred surface, while the pristine PDMS was ranked as the least preferred by 60% of the participants.

Besides their effect on haptics, self-assembled amphiphiles alter triboelectric signals in largely unexplored ways (*23*, *55*). Triboelectrification arises from a robust electron cloud overlap between tribolayers, where atomic-level contact is established with an interatomic distance shorter than the bonding length (*56*). Sliding friction and adhesion both facilitate an increased electron cloud overlap (*7*, *56*, *57*). Efficient electron transfer between the tribopairs can also be achieved by tuning the electronegativity of the surface (*58*). To test these approaches for triboelectric manipulation, we examined self-assembled amphiphilic layers of stearic acid (SA) and 1*H*,1*H*-perfluorooctyl amine (F-NH_2) (see Materials and Methods), in addition to the aliphatic amides, due to their propensity to enhance the electronegativity of the polymeric tribolayer (*17*, *23*). The triboelectric performance of pristine and coated PDMS substrates was assessed using a Cu/PDMS/Cu triboelectric device in contact-separation mode on a mechanical tester (Fig. 4C and Materials and Methods). Cyclic contact generated positive charges on Cu and negative charges on PDMS. The induced charge separation led to a measurable current (I_{SC}) and charge density (σ_{SC}) under short-circuit conditions and a voltage drop (V_{OC}) under open-circuit conditions.

Figure 4 (D and E) and fig. S17 show that all self-assembled layers generate stable, consistent, and distinct triboelectric signals compared to the pristine PDMS surface, highlighting their ability to tune triboelectric properties effectively. For instance, while pristine PDMS exhibits a peak V_{OC} value of 98.3 V, layers of fluorooctylamine, SA, BE, and ER produced V_{OC} values of 314.4, 241.2, 69.89, and 13.8 V under a nominal contact pressure of 0.03 MPa. Finger tapping at a lower normal load produced similar trends as the mechanical tester (Fig. 4, F and G, and movie S2). In addition, fig. S18 shows that the triboelectric outputs for the amphiphile-coated PDMS are dependent on the contact pressure P, similar to their frictional properties (Fig. 3). V_{OC} signals increase with increase in P, particularly at low pressures (<0.1 MPa) relevant for wearable applications (*59*). This pressure dependence likely originates from the evolution of the real contact area with contact pressure, where atomic-level contact and electron cloud overlap can be established between the tribolayers, until it approaches the nominal contact area where the triboelectric signals saturate (*59*).

The observed differences in the triboelectric output between the different amphiphiles stem from a balance between their ability to reduce adhesive frictional contact (*7*) and their potential to enhance the electron-withdrawing ability (*58*) of PDMS and, in turn, the charge transfer density (ST section 8). Figure 4H shows the proposed molecular mechanism of triboelectric tuning by the amphiphiles. Pristine PDMS is a tribo-negative layer and forms negative surface charges during contact with the Cu substrate. The corresponding electrostatic induction results in dipoles that are aligned in the upward direction (*60*). Aliphatic amides may have a lower electron-withdrawing capacity compared to PDMS, and therefore reduce the negative surface charges and partially misalign the dipole direction, reducing polarization and output (*58*, *60*). SA and fluorooctylamine layers, however, further increase the surface charge due to their enhanced electron-withdrawing ability with the dipoles aligned in the same direction as PDMS, increasing polarization and hence the triboelectric output (*17*, *23*, *60*). This ability to tune the triboelectric output through interfacial modification is sustained over more than 80 contact-separation cycles while maintaining performance (fig. S19) and, therefore, holds potential for applications in intelligent haptic communication and sensing devices (*4*, *13*). Overall, Fig. 4 shows that an appropriate slip additive blend is crucial not just for maximizing performance but also for ensuring tactile comfort of wearable devices during prolonged contact against bare skin (*2*, *4*, *6*, *9*).

DISCUSSION

This study demonstrates the facile use of interfacial modification of soft materials by means of using small self-assembled amphiphiles to tune energy harvesters that are haptically distinct with tunable triboelectric output. The interplay between the applied pressure, molecular structure, and electron affinity, as well as substrate compliance collectively informs the friction reduction, tactile perception, and triboelectric performance of the amphiphile-coated materials. We provide a framework that connects the molecular organization of two amide-based amphiphiles that differ only in a single C═C bond to the applied pressure. The scaling shows that friction reduction increases with pressure under low pressures and is maximized primarily at high pressures due to the pressure-induced formation of multiple slip layers. Crucially, friction reduction is limited by the inherent properties of these interfacial layers rather than that of the bulk materials in contact.

Notable differences in tactile perception experienced by humans, as shown here with pristine and amphiphile-coated soft materials, are useful in enhancing user experience in real-world applications where wearable energy harvesters must remain in contact with human skin for extended durations (*6*, *9*). This haptic comfort should be balanced with the triboelectric performance through the electron affinity and frictional properties of the self-assembled amphiphiles. With ever-increasing device performance in the fields of self-powered electronic skins and haptic communication systems (*4*), physicochemical enhancement of user experience is likely to become critical design parameters for future generations of consumer electronics, biomedical devices (*14*), and wearable technology (*6*, *61*).

MATERIALS AND METHODS

Substrate preparation

PP (thickness of 1.5 mm, McMaster-Carr), LDPE (thickness of 1.5 mm, US Plastic Corporation), and Si wafer (thickness = of 1 mm, University Wafer) were cut into 15 mm–by–6 mm rectangular slabs for tribological characterization. The slabs were cleaned under sonication in acetone, isopropanol, and water for 10 min each successively followed by drying using a nitrogen gun. Fifty microliters of 1% w/v solution of ER (TCI America) in isopropanol was drop casted onto preheated PP and LDPE slabs at 80°C to achieve uniform distribution and promote adhesion of ER with the substrates. The slabs were dried in ambient conditions for 2 days before tribology tests. Coated Si wafer slabs were prepared similarly with 50 μl of 1% w/v ER-toluene solution under ambient conditions. ER-coated PDMS slabs were prepared via a modified protocol reported by Seo *et al.* (*35*). Briefly, 11 g of Sylgard 184 (Dow Corning) with a base to curing agent ratio of 10:1 w/w was mixed and deaerated in a vortex mixer (Thinky Mixer, ARE-310) followed by the addition of 5 ml of 2% w/v ER-toluene solution and mixing-deaeration steps. The composite PDMS (thickness of 1.2 mm) was cured at 65°C overnight in a vacuum oven to allow removal of toluene. Pristine PDMS substrates were prepared similarly without the addition of the ER solution. A PP nonwoven fabric, (16 ± 2 g/m^2, thickness of 0.15 mm, Fibertex Personal Care Malaysia) used as topsheet in hygiene products, was cut into 50 mm–by–50 mm square patches and incubated in 5 ml of 1% w/v ER-isopropanol solution at 80°C for 180 min to achieve complete coverage of the slip additive followed by drying in ambient conditions over 2 days. BE (TCI America)–coated PP and PDMS slabs were prepared through identical solvent-assisted casting protocols as ER-coated slabs. SA-coated PDMS slabs were prepared by spin coating from a 1% w/v solution in dimethyl sulfoxide followed by drying under ambient conditions. 1*H*,1*H*-perfluorooctylamine-coated PDMS slabs were prepared by spin coating (1000 rpm, 30 s) a 0.5% w/v solution of the fluoro-additive in dimethyl sulfoxide with 10% v/v acetic acid to protonate the amine groups. The coated slabs were dried under a closed petri dish for 14 hours to allow electrostatic self-assembly of the perfluoro molecules on the PDMS surface (*17*). Before spin coating, the PDMS slabs were subjected to ultraviolet-ozone treatment for 30 min to remove any surface contaminants.

ER detection using ATR-FTIR spectroscopy

To confirm the presence of the ER interfacial layer post substrate preparation, attenuated total reflectance Fourier transform infrared

(ATR-FTIR) spectroscopy (Bruker, diamond crystal) was performed in the solid state on both coated and pristine substrates. Infrared spectra were collected over 32 scans with a 4 cm^{-1} resolution from 4000 to 650 cm^{-1}.

Tribopair surface roughness

The root mean square height (S_q) roughness for the pristine, ER-coated, and BE-coated substrates as well as the counter bodies of PP ball, PDMS ball, and polyurethane skin simulant was measured by optical profilometry using confocal laser scanning microscopy (Keyence VKx1000). Three-dimensional (3D) surface topography images and surface roughness measurements were collected using a 20× dry objective [numerical aperture (NA) of 0.46] through reflectance mode imaging over a scanning area of 527 μm by 703 μm at three different spots on each substrate, and the average S_q was reported.

Young's modulus (*E*) determination for LDPE, PDMS, and PP nonwoven

To determine the substrate modulus, tensile testing (Intron 5943) was performed for LDPE, PDMS, and PP nonwoven substrates. Substrates were cut into dimensions of 75 mm by 25 mm and stretched uniaxially at 50 mm/min. The Young's modulus, E, was calculated from the slope of linear Hookean regime of the stress-strain curve below a strain of 0.03 mm/mm. The E values were averaged over two replicates for LDPE and PDMS and over five replicates for PP nonwovens. For PP and Si wafer, E values were obtained from the literature (table S1).

Friction measurements

PP, LDPE, Si wafer, and PDMS substrates

Dry friction experiments were performed on a stress-controlled triborheometer (HR20, TA Instruments) with a ball-on-three-plates geometry. The geometry consists of a 0.5-inch (0.0127-m) ball attached at the top and three rectangular slots at 45° to the horizontal plane where the test slabs were placed (fig. S4A). The balls used were either PP (McMaster-Carr) or PDMS spheres and were fabricated using a custom stainless-steel mold. Before testing, the reference zero gap was set by measuring a finite normal load when the two materials were slowly pushed into solid contact. The three test slabs were then placed in the slots, and the ball was lowered until the desired normal load was reached. Normal loads in the range of 0.7 to 35.3 N were evaluated across different tribopair combinations (table S2). All friction tests were performed in dry conditions at a constant sliding speed of 5 mm/s for 3600 s. To ensure stability and minimal movement of the test slabs in the slots, a double-sided tape was used to hold the slabs in place during measurements. Tests were performed in triplicates for each set of pristine and slip additive-coated substrates.

Polyurethane-PP nonwoven tribopair to simulate fabric-skin contact

Tribological characterization was performed with a ring-on-plate geometry (fig. S5A) where an annular stainless-steel ring (inner diameter of 29 mm and outer diameter of 32 mm) was attached at the top onto which the PP nonwoven patch was taped. The bottom plate consisted of a polyurethane elastomer–based skin simulant (thickness of 5 mm, Beaulax Japan). The annular ring with the PP nonwoven patch was first used to zero the gap with the bottom plate. Thereafter, the frictional response was measured under $F_N = 1.4$ N with a sliding speed of 5 mm/s for 900 s (fig. S5). Tests were performed in triplicates with and without the ER coating.

Contact area measurements

Stiff tribopairs (PP-PP, PP-LDPE, and PP-Si wafer)

Confocal scanning laser microscopy (Keyence VKx1100) was used to obtain A_c values for PP, LDPE, and Si wafer slabs after cessation of shear at $t = 3600$ s. The contact areas were imaged using a 20× dry objective (NA of 0.46) and the auto 3D laser scanning mode with a 404-nm violet laser source. Nine images (483 μm by 644 μm each) were stitched to obtain one composite image (Fig. 2H and figs. S8, A to C, and S9A). The stitched images were corrected for plane tilt, and the 2D contact radius (a) was obtained using the edge and radius detection tools of the Keyence MultiFileAnalyzer software. Contact area measurements ($A_c = \pi a^2$) for pristine, ER-coated, and BE-coated tribopair were conducted with three independent samples. An exception was the pristine Si wafer slabs because no detectable contact was visualized after the tribology tests. Contact area images displayed in this study were pseudo-colored images acquired after applying the LUT filter (RedHot) to the confocal laser images in Fiji.

Soft tribopairs (PP-PDMS and PDMS-PDMS)

For PDMS slabs, contact areas were visualized by compression testing on the rheometer using a modified protocol reported by Peng *et al.* (*12*). Briefly, fluorescent Nile Red (Millipore Sigma) dissolved in isopropanol (1:10 w/w) was used to dye the PP and PDMS spheres. A dyed ball was then attached to the top part of the ball-on-three-plates geometry and lowered to press against the undyed ER-coated substrates at a constant normal load equal to that of the friction tests for 5 min in static condition to allow sphere-to-substrate dye transfer. The resulting fluorescent contact area was then visualized using a confocal inverted microscope (Leica TCS SP8) with a 10× dry objective, and tile stitching was performed to obtain a 7.65 mm–by–7.65 mm composite image. Although the static contact area is likely to differ from the actual contact area during sliding, where it is expected to decrease under shear (*62*), our approach provides a first-order approximation of the contact area under sliding (*12*). The stitched images were post-processed in Fiji with a Gaussian blur filter (kernel size $\sigma = 0.01$ mm) and thenc auto thresholded to quantify the contact area.

Grazing-incidence x-ray scattering

Grazing-incidence x-ray scattering, a highly surface-sensitive technique, was performed on ER- and BE-coated PDMS substrates on a Xeuss 3.0 (XENOCS, France) system that enabled the accurate determination of ordered structures formed at the surface of a material. The system is equipped with a Genix 3D (Cu-Kα) x-ray radiation source and a Pilatus3R 300 K detector (Dectris, Switzerland). The grazing-incidence angle was set at 0.15°. Experiments were performed under vacuum spanning a wave vector range of 10^{-3} Å$^{-1} \leq q \leq 3.4$ Å^{-1}.

Human tactile perception trials with 3-AFC

Five volunteers ranging from 21 to 30 years old participated in the study. The study was conducted with the approval of the Institutional Review Board at the University of Delaware (IRBNet ID#: 1484385-5), and the participants gave their informed consent before the procedure. Participants were blindfolded and used their dominant index finger to freely explore each sample in a given comparison pair of PDMS substrates (thickness of 1.2 mm) in the 3-AFC trial.

Triboelectric device fabrication and characterization

The triboelectric performance of pristine, ER-coated, BE-coated, SA-coated, and F-NH_2–coated PDMS substrates was evaluated using vertical contact-separation mode triboelectric device. For Cu/PDMS/Cu triboelectric devices, Cu sheets were selected as the positive tribolayer and the collecting electrode, and 1-mm-thick PDMS slabs served as the negative tribolayer. Dimensions of all triboelectric devices were 50 mm by 50 mm with 10 mm as the separation distance between the Cu and PDMS layers. Ten vertical oscillation cycles were performed using a linear reciprocating motor at constant frequency of 0.3 Hz at an apparent pressure of 0.03 MPa during contact. Similar measurements were conducted for the skin/PDMS/Cu triboelectric setup with 10 finger taps on the PDMS slab at regular intervals. Pressure dependence of V_{OC} for ER-coated and BE-coated PDMS devices was measured by running the experiments under difference normal loads $F_N = 12.5$, 25, 33.5, 42.5, and 70 N. Stability of the self-assembled layers was assessed by recording V_{OC} and I_{SC} signals over 80 continuous oscillation cycles at $P = 0.03$ MPa. V_{OC}, I_{SC}, and Q_{SC} signals were continuously recorded with an electrometer (Keithley 6514). An oscilloscope (PicoScope 2000) was used to measure the V_{OC} of the F-NH_2–coated device. All measurements were performed in triplicates at $T = 22$°C and 49% relative humidity.

Supplementary Materials

The PDF file includes:

Supplementary Text
Figs. S1 to S20
Tables S1 to S3
Legends for movies S1 and S2
References

Other Supplementary Material for this manuscript includes the following:

Movies S1 and S2

REFERENCES AND NOTES

1. V. Nair, A. N. Dalrymple, Z. Yu, G. Balakrishnan, C. J. Bettinger, D. J. Weber, K. Yang, J. T. Robinson, Miniature battery-free bioelectronics. *Science* **382**, eabn4732 (2023).
2. X. Yu, Z. Xie, Y. Yu, J. Lee, A. Vazquez-Guardado, H. Luan, J. Ruban, X. Ning, A. Akhtar, D. Li, B. Ji, Y. Liu, R. Sun, J. Cao, Q. Huo, Y. Zhong, C. M. Lee, S. Y. Kim, P. Gutruf, C. Zhang, Y. Xue, Q. Guo, A. Chempakasseril, P. Tian, W. Lu, J. Y. Jeong, Y. J. Yu, J. Cornman, C. S. Tan, B. H. Kim, K. H. Lee, X. Feng, Y. Huang, J. A. Rogers, Skin-integrated wireless haptic interfaces for virtual and augmented reality. *Nature* **575**, 473–479 (2019).
3. S. M. Won, E. Song, J. T. Reeder, J. A. Rogers, Emerging modalities and implantable technologies for neuromodulation. *Cell* **181**, 115–135 (2020).
4. W. Wang, Y. Jiang, D. Zhong, Z. Zhang, S. Choudhury, J.-C. Lai, H. Gong, S. Niu, X. Yan, Y. Zheng, C.-C. Shih, R. Ning, Q. Lin, D. Li, Y.-H. Kim, J. Kim, Y.-X. Wang, C. Zhao, C. Xu, X. Ji, Y. Nishio, H. Lyu, J. B. H. Tok, Z. Bao, Neuromorphic sensorimotor loop embodied by monolithically integrated, low-voltage, soft e-skin. *Science* **380**, 735–742 (2023).
5. X. Qu, Z. Liu, P. Tan, C. Wang, Y. Liu, H. Feng, D. Luo, Z. Li, Z. Lin Wang, Artificial tactile perception smart finger for material identification based on triboelectric sensing. *Sci. Adv.* **8**, eabq2521 (2022).
6. H. Fang, J. Guo, H. Wu, Wearable triboelectric devices for haptic perception and VR/AR applications. *Nano Energy* **96**, 107112 (2022).
7. D. W. Kim, J. H. Lee, J. K. Kim, U. Jeong, Material aspects of triboelectric energy generation and sensors. *NPG Asia Mater.* **12**, 6 (2020).
8. L. Zhang, H. Cai, L. Xu, L. Ji, D. Wang, Y. Zheng, Y. Feng, X. Sui, Y. Guo, W. Guo, F. Zhou, W. Liu, Z. L. Wang, Macro-superlubric triboelectric nanogenerator based on tribovoltaic effect. *Matter* **5**, 1532–1546 (2022).
9. T. Shimura, S. Sato, P. Zalar, N. Matsuhisa, Engineering the comfort-of-wear for next generation wearables. *Adv. Electron. Mater.* **9**, 2200512 (2023).
10. A. Klöcker, M. Wiertlewski, V. Théate, V. Hayward, J. L. Thonnard, Physical factors influencing pleasant touch during tactile exploration. *PLOS ONE* **8**, e79085 (2013).
11. K. L. Harris, E. S. Collier, L. Skedung, M. W. Rutland, A sticky situation or rough going? Influencing haptic perception of wood coatings through frictional and topographical design. *Tribol. Lett.* **69**, 113 (2021).
12. Y. Peng, C. M. Serfass, A. Kawazoe, Y. Shao, K. Gutierrez, C. N. Hill, V. J. Santos, Y. Visell, L. C. Hsiao, Elastohydrodynamic friction of robotic and human fingers on soft micropatterned substrates. *Nat. Mater.* **20**, 1707–1711 (2021).
13. C. W. Carpenter, C. Dhong, N. B. Root, D. Rodriquez, E. E. Abdo, K. Skelil, M. A. Alkhadra, J. Ramírez, V. S. Ramachandran, D. J. Lipomi, Human ability to discriminate surface chemistry by touch. *Mater. Horiz.* **5**, 70–77 (2018).
14. D. J. Lipomi, C. Dhong, C. W. Carpenter, N. B. Root, V. S. Ramachandran, Organic haptics: Intersection of materials chemistry and tactile perception. *Adv. Funct. Mater.* **30**, 1906850 (2020).
15. E. Liamas, S. D. Connell, S. N. Ramakrishna, A. Sarkar, Probing the frictional properties of soft materials at the nanoscale. *Nanoscale* **12**, 2292–2308 (2020).
16. H. Spikes, Friction modifier additives. *Tribol. Lett.* **60**, 5 (2015).
17. J. R. Yang, C. J. Lee, C. Y. Chang, An electrostatically self-assembled fluorinated molecule as a surface modification layer for a high-performance and stable triboelectric nanogenerator. *J. Mater. Chem. A Mater.* **9**, 4230–4239 (2021).
18. A. Nolin, A. Licht, K. Pierson, C. Y. Lo, L. V. Kayser, C. Dhong, Predicting human touch sensitivity to single atom substitutions in surface monolayers for molecular control in tactile interfaces. *Soft Matter* **17**, 5050–5060 (2021).
19. T. Jia, H. Tian, S. Liu, S. Zhang, N. Ning, B. Yu, M. Tian, Erucamide/thermoplastic polyurethane blend with low coefficient of friction, high elasticity and good mechanical properties for intelligent wearable devices. *Polym. Int.* **72**, 813–821 (2023).
20. M. X. Ramírez, D. E. Hirt, L. L. Wright, AFM characterization of surface segregated erucamide and behenamide in linear low density polyethylene film. *Nano Lett.* **2**, 9–12 (2002).
21. Z. Zachariah, P. C. Nalam, A. Ravindra, A. Raju, A. Mohanlal, K. Wang, R. V. Castillo, R. M. Espinosa-Marzal, Correlation between the adsorption and the nanotribological performance of fatty acid-based organic friction modifiers on stainless steel. *Tribol. Lett.* **68**, 11 (2020).
22. F. Abouhadid, A. Crespo, N. Morgado, D. Mazuyer, J. Cayer-Barrioz, Friction Laws for Saturated/Unsaturated Fatty Acid Layers. *Tribol. Lett.* **69**, 46 (2021).
23. S. Shen, Y. Zhao, R. Cao, H. Wu, W. Zhang, Y. Zhu, K. Ren, C. Pan, Triboelectric polymer with excellent enhanced electrical output performance over a wide temperature range. *Nano Energy* **110**, 108347 (2023).
24. T. W. Scharf, S. V. Prasad, Solid lubricants: A review. *J. Mater. Sci.* **48**, 511–531 (2013).
25. D. Gubała, N. Taylor, R. Harniman, J. Rawle, H. Hussain, E. Robles, M. Chen, W. H. Briscoe, Structure, nanomechanical properties, and wettability of organized erucamide layers on a polypropylene surface. *Langmuir* **37**, 6521–6532 (2021).
26. J. P. Ewen, S. K. Kannam, B. D. Todd, D. Dini, Slip of alkanes confined between surfactant monolayers adsorbed on solid surfaces. *Langmuir* **34**, 3864–3873 (2018).
27. W. Lin, M. Kluzek, N. Iuster, E. Shimoni, N. Kampf, R. Goldberg, J. Klein, Cartilage-inspired, lipid-based boundary-lubricated hydrogels. *Science* **370**, 335–338 (2020).
28. J. D. Hernández Velázquez, J. Barroso-Flores, A. Gama Goicochea, Ab initio modeling of friction reducing agents shows quantum mechanical interactions can have macroscopic manifestation. *J. Phys. Chem. A* **120**, 9244–9248 (2016).
29. B. Derjaguin, Untersuchungen über die Reibung und Adhäsion, IV. *Kolloid-Zeitschrift* **69**, 155–164 (1934).
30. F. P. Bowden, J. N. Gregory, D. Tabor, Lubrication of metal surfaces by fatty acids. *Nature* **156**, 97–101 (1945).
31. O. Piétrement, M. Troyon, Study of the interfacial shear strength pressure dependence by modulated lateral force microscopy. *Langmuir* **17**, 6540–6546 (2001).
32. J. Gao, W. D. Luedtke, D. Gourdon, M. Ruths, J. N. Israelachvili, U. Landman, Frictional forces and Amontons' law: From the molecular to the macroscopic scale. *J. Phys. Chem. B* **108**, 3410–3425 (2004).
33. J. P. Ewen, C. Gattinoni, N. Morgan, H. A. Spikes, D. Dini, Nonequilibrium molecular dynamics simulations of organic friction modifiers adsorbed on iron oxide surfaces. *Langmuir* **32**, 4450–4463 (2016).
34. B. V. Farias, S. A. Khan, Probing gels and emulsions using large-amplitude oscillatory shear and frictional studies with soft substrate skin surrogates. *Colloids Surf. B Biointerfaces* **201**, 111595 (2021).
35. E. Seo, J. W. Lee, D. Lee, M. R. Seong, G. H. Kim, D. S. Hwang, S. J. Lee, Eco-friendly erucamide–polydimethylsiloxane coatings for marine anti-biofouling. *Colloids Surf. B Biointerfaces* **207**, 112003 (2021).
36. B. N. J. Persson, I. M. Sivebaek, V. N. Samoilov, K. Zhao, A. I. Volokitin, Z. Zhang, On the origin of Amonton's friction law. *J. Phys. Condens. Matter* **20**, 395006 (2008).
37. B. Weber, T. Suhina, T. Junge, L. Pastewka, A. M. Brouwer, D. Bonn, Molecular probes reveal deviations from Amontons' law in multi-asperity frictional contacts. *Nat. Commun.* **9**, 888 (2018).
38. A. R. Kim, A. Cholewinski, S. K. Mitra, B. Zhao, Viscoelastic tribopairs in dry and lubricated sliding friction. *Soft Matter* **16**, 7447–7457 (2020).
39. C. Myant, H. A. Spikes, J. R. Stokes, Influence of load and elastic properties on the rolling and sliding friction of lubricated compliant contacts. *Tribol. Int.* **43**, 55–63 (2010).
40. X. He, Z. Liu, L. B. Ripley, V. L. Swensen, I. J. Griffin-Wiesner, B. R. Gulner, G. R. McAndrews, R. J. Wieser, B. P. Borovsky, Q. J. Wang, S. H. Kim, Empirical relationship between interfacial

shear stress and contact pressure in micro- and macro-scale friction. *Tribol. Int.* **155**, 106780 (2021).
41. M. Ruths, S. Lundgren, K. Danerlöv, K. Persson, Friction of fatty acids in nanometer-sized contacts of different adhesive strength. *Langmuir* **24**, 1509–1516 (2008).
42. D. Gubała, L. J. Fox, R. Harniman, H. Hussain, E. Robles, M. Chen, W. H. Briscoe, Heads or tails: Nanostructure and molecular orientations in organised erucamide surface layers. *J. Colloid Interface Sci.* **590**, 506–517 (2021).
43. J. S. Bhamra, J. P. Ewen, C. A. Latorre, J. A. R. Bomidi, M. W. Bird, N. Dasgupta, A. C. T. Van Duin, D. Dini, Interfacial bonding controls friction in diamond-rock contacts. *J. Phys. Chem. C* **125**, 18395–18408 (2021).
44. T. Mishra, M. de Rooij, M. Shisode, J. Hazrati, D. J. Schipper, Characterization of interfacial shear strength and its effect on ploughing behaviour in single-asperity sliding. *Wear* **436-437**, 203042 (2019).
45. B. J. Briscoe, D. C. B. Evans, The shear properties of Langmuir-Blodgett layers. *Proc. R. Soc. Lond. A.* **380**, 389–407 (1982).
46. H. Song, L. Ji, H. Li, J. Wang, X. Liu, H. Zhou, J. Chen, Self-forming oriented layer slip and macroscale super-low friction of graphene. *Appl. Phys. Lett.* **110**, 073101 (2017).
47. Y. Meng, J. Sun, J. He, F. Yang, P. Wu, Interfacial interaction induced synergistic lubricating performance of MoS_2 and SiO_2 composite nanofluid. *Colloids Surf. A Physicochem. Eng. Asp.* **626**, 126999 (2021).
48. Ł. Baran, P. Llombart, W. Rżysko, L. G. MacDowell, Ice friction at the nanoscale. *Proc. Natl. Acad. Sci. U.S.A.* **119**, 1–7 (2022).
49. M. Mansha, C. Gauthier, P. Gerard, R. Schirrer, The effect of plasticization by fatty acid amides on the scratch resistance of PMMA. *Wear* **271**, 671–679 (2011).
50. F. Ali, Numerical study on subsurface stress in Hertzian contacts under pure sliding conditions. *J. Appl. Comput. Mech.* **6**, 1098–1106 (2020).
51. J. Zhang, Y. Meng, Boundary lubrication by adsorption film. *Friction* **3**, 115–147 (2015).
52. C. Pacchierotti, S. Sinclair, M. Solazzi, A. Frisoli, V. Hayward, D. Prattichizzo, Wearable haptic systems for the fingertip and the hand: Taxonomy, review, and perspectives. *IEEE Trans. Haptics* **10**, 580–600 (2017).
53. L. Willemet, K. Kanzari, J. Monnoyer, I. Birznieks, M. Wiertlewski, Initial contact shapes the perception of friction. *Proc. Natl. Acad. Sci. U.S.A.* **118**, e2109109118 (2021).
54. B. M. Dzidek, M. J. Adams, J. W. Andrews, Z. Zhang, S. A. Johnson, Contact mechanics of the human finger pad under compressive loads. *J. R. Soc. Interface* **14**, 20160935 (2017).
55. J. Zhang, Y. Zheng, L. Xu, D. Wang, Oleic-acid enhanced triboelectric nanogenerator with high output performance and wear resistance. *Nano Energy* **69**, 104435 (2020).
56. Z. L. Wang, A. C. Wang, On the origin of contact-electrification. *Mater. Today* **30**, 34–51 (2019).
57. Y. Yu, Q. Gao, X. Zhang, D. Zhao, X. Xia, J. Wang, H. Li, Z. L. Wang, T. Cheng, Contact-sliding-separation mode triboelectric nanogenerator. *Energ. Environ. Sci.* **16**, 3932–3941 (2023).
58. Y. Shang, Z. Wang, C. Yu, W. Xu, Z. Chen, B. Jiang, H. Zhang, Chemical structure-based design of triboelectric materials for high-performance TENGs. *Nano Energy* **103**, 107847 (2022).
59. Y. Xu, G. Min, N. Gadegaard, R. Dahiya, D. M. Mulvihill, A unified contact force-dependent model for triboelectric nanogenerators accounting for surface roughness. *Nano Energy* **76**, 105067 (2020).
60. W. Kim, J. H. Park, H. J. Hwang, Y. S. Rim, D. Choi, Interfacial molecular engineering for enhanced polarization of negative tribo-materials. *Nano Energy* **96**, 107110 (2022).
61. P. Uttayopas, X. Cheng, J. Eden, E. Burdet, Object recognition using mechanical impact, viscoelasticity, and surface friction during interaction. *IEEE Trans. Haptics* **16**, 251–260 (2023).
62. R. Sahli, G. Pallares, C. Ducottet, I. E. Ben Ali, S. Al Akhrass, M. Guibert, J. Scheibert, Evolution of real contact area under shear and the value of static friction of soft materials. *Proc. Natl. Acad. Sci. U.S.A.* **115**, 471–476 (2018).
63. D. J. Cottenden, A. M. Cottenden, A study of friction mechanisms between a surrogate skin (Lorica soft) and nonwoven fabrics. *J. Mech. Behav. Biomed. Mater.* **28**, 410–426 (2013).
64. H. Zeng, *Polymer Adhesion, Friction and Lubrication* (John Wiley & Sons Ltd., 2013).
65. K. L. Johnson, K. Kendall, A. D. Roberts, Surface energy and the contact of elastic solids. *Proc. R. Soc. Lond. A.* **324**, 301–313 (1971).
66. D. K. Owens, R. C. Wendt, Estimation of the surface free energy of polymers. *J. Appl. Polym. Sci.* **13**, 1741–1747 (1969).
67. Z. Zhang, W. Wang, A. N. Korpacz, C. R. Dufour, Z. J. Weiland, C. R. Lambert, M. T. Timko, Binary liquid mixture contact-angle measurements for precise estimation of surface free energy. *Langmuir* **35**, 12317–12325 (2019).
68. H. Zou, Y. Zhang, L. Guo, P. Wang, X. He, G. Dai, H. Zheng, C. Chen, A. C. Wang, C. Xu, Z. L. Wang, Quantifying the triboelectric series. *Nat. Commun.* **10**, 1427 (2019).
69. M. Kumar, K. K. Gaur, C. Shaker, Measurement of material constants (Young's modulus and Poisson's ratio) of polypropylene using digital speckle pattern interferometry (DSPI). *J. Japan. Soc. Experiment. Mech.* **15**, s87–s91 (2015).
70. M. A. Hopcroft, W. D. Nix, T. W. Kenny, What is the Young's modulus of silicon? *J. Microelectromech. Syst.* **19**, 229–238 (2010).
71. N. H. Ladizesky, I. M. Ward, Determination of Poisson's ratio and Young's modulus of low-density polyethylene. *J. Macromole. Sci. B* **5**, 661–692 (1971).
72. A. Müller, M. C. Wapler, U. Wallrabe, A quick and accurate method to determine the Poisson's ratio and the coefficient of thermal expansion of PDMS. *Soft Matter* **15**, 779–784 (2019).
73. K. E. Spear, J. P. Dismukes, *Synthetic Diamond: Emerging CVD Science and Technology* (Wiley, 1994).

Acknowledgments: We thank M. Dickey and F. Castellano for mechanical, triboelectric, and ATR-FTIR characterization tools, J. Genzer for scientific discussions, and Fibertex Personal Care Malaysia for providing nonwoven fabrics. This work was performed, in part, at the Analytical Instrumentation Facility (AIF) at North Carolina State University, which is supported by the State of North Carolina and the NSF (ECCS-2025064). **Funding:** This work was supported by the Nonwovens Institute, project 18-224SB (S.A.K.); NSF CAREER, award CBET-2042635 (L.C.H.); Sloan Research Fellowship, FG-2022-18336 (L.C.H.); Dreyfus Foundation, TC-22-038 (L.C.H.); National Institutes of Health, grant R01EY032584-02 (C.D.); and NIH National Eye Institute, grant 5R01EY032584-03 (C.D.). **Author contributions:** L.C.H. and S.A.K. conceived and designed the study. P.K.J. carried out friction, microscopy, and triboelectric experiments. K.Y. conducted triboelectric experiments. H.K. and L.C.H. conducted and analyzed x-ray scattering data. M.D. conducted human psychophysical tests for tactile perception. L.C.H., P.K.J., C.D., and M.D. analyzed and interpreted experimental data. All authors cowrote the manuscript. **Competing interests:** The authors declare that they have no competing interests. **Data and materials availability:** All data needed to evaluate the conclusions in the paper are present in the paper and/or the Supplementary Materials.

Submitted 2 July 2024
Accepted 13 December 2024
Published 15 January 2025
10.1126/sciadv.adr4088